



Optimization of Material Contrast for Efficient FIB-SEM Tomography of Solid Oxide Fuel Cells

M. Meffert^{1*}, F. Wankmüller², H. Störmer¹, A. Weber², P. Lupetin³, E. Ivers-Tiffée², D. Gerthsen¹

¹ Karlsruhe Institut für Technologie (KIT), Laboratorium für Elektronenmikroskopie, Engesserstraße 7, 76131 Karlsruhe, Germany

² Karlsruhe Institut für Technologie (KIT), Institut für Angewandte Materialien - Werkstoffe der Elektrotechnik (IAM-WET), Adenauerring 20b, 76131 Karlsruhe, Germany

³ Robert Bosch GmbH, Corporate Sector Research and Advance Engineering, Robert-Bosch-Campus 1, 71272 Renningen, Germany.

Received June 30, 2020; accepted August 25, 2020; published online October 01, 2020

Abstract

Focused ion beam (FIB) – scanning electron microscopy (SEM) serial sectioning tomography has become an important tool for three-dimensional microstructure reconstruction of solid oxide fuel cells (SOFC) to obtain an understanding of fabrication-related effects and SOFC performance. By sequential FIB milling and SEM imaging a stack of cross-section images across all functional SOFC layers was generated covering a large volume of $3.5 \cdot 10^4 \mu\text{m}^3$. One crucial step is image segmentation where regions with different image intensities are assigned to different material phases within the SOFC. To analyze all relevant SOFC materials, it was up to now mandatory to acquire several images by scanning the same region with different imaging parameters because sufficient material

contrast could otherwise not be achieved. In this work we obtained high-contrast SEM images from a single scan to reconstruct all functional SOFC layers consisting of a Ni/Y₂O₃-doped ZrO₂ (YDZ) cermet anode, YDZ electrolyte and (La,Sr)MnO₃/YDZ cathode. This was possible by using different, simultaneous read-out detectors installed in a state-of-the-art scanning electron microscope. In addition, we used a deterministic approach for the optimization of imaging parameters by employing Monte Carlo simulations rather than trial-and-error tests. We also studied the effect of detection geometry, detecting angle range and detector type.

Keywords: Backscattered Electron, Detectors, FIB-SEM Tomography, Material Contrast, Secondary Electron, Solid Oxide Fuel Cell

1 Introduction

Solid oxide fuel cells (SOFCs) are attractive devices for the conversion of chemical into electrical energy. High conversion efficiency, combustion-less operation and fuel flexibility make SOFCs highly interesting in the field of combined heat and power generation [1]. Although SOFCs have been investigated for decades, there is still a considerable need for microstructure optimization, even if well-established SOFC materials and fabrication technologies are used. Scanning electron microscopy (SEM) has been an essential technique to elucidate the SOFC microstructure and correlate microstructure with electrochemical properties and fabrication parameters. However, not all relevant parameters of the SOFC microstructure can be quantitatively measured based on single SEM images. The determination of important properties like tortuosity and triple phase boundary (TPB) length in the porous SOFC

cathode and anode requires reconstruction of the three-dimensional (3D) microstructure. An established technique for this purpose is focused ion beam (FIB)-SEM serial sectioning tomography, which allows to reconstruct the 3D microstructure with a spatial resolution in the few 10 nm range and extract performance-relevant cell parameters [2–7]. In FIB-SEM tomography, a series of alternating FIB milling and SEM imaging steps produces a set of images through a chosen sample volume. Single images can be decomposed into regions containing different materials if materials exhibit different SEM

[*] Corresponding author, matthias.meffert@kit.edu

 This is an open access article under the terms of the Creative Commons Attribution License, which permits use, distribution and reproduction in any medium, provided the original work is properly cited.

intensities. Hence, reliable segmentation of different phases and consecutive 3D reconstruction requires high contrast between different materials. Therefore, it is essential to optimize material contrast by selecting adequate parameters for SEM imaging.

In SEM, common electron signals can be divided into secondary electron (SE) and backscattered electron (BSE) signals. SEs with low energies (by definition < 50 eV) can only exit from the sample if they are generated close to the specimen surface. Therefore, SE image intensity is governed by the local surface tilt with respect to the incident electron beam yielding mainly topography contrast with only minor contributions from the material composition. BSEs with higher electron energies are predominantly generated by few elastic scattering events, which leads to a strong dependence on the chemical composition and only to a lesser degree on surface topography. The image intensity is generally assessed by the SE or BSE coefficients, which are defined by the number of generated SE or BSE per primary electron, respectively. An empirical equation for the BSE coefficient η is given by

$$\eta = (1 + \cos\varphi) \frac{-9}{\sqrt{Z}} \quad (1)$$

with the average atomic number of the material Z and the angle between primary electron beam and specimen surface φ [32]. The pronounced dependence of the BSE intensity on chemical composition makes BSE SEM imaging well suited to distinguish phases with different chemical compositions. However, some commonly used SOFC materials exhibit weak material contrast because their average atomic numbers are similar. This applies, e.g., to $(\text{La}, \text{Sr})\text{MnO}_3$ (LSM) and Y_2O_3 -doped ZrO_2 (YDZ), which are commonly used in SOFC cathodes [4, 5, 8–10]. In some instances, SE SEM imaging at low electron energies (0.6–2 keV) and employing an in-lens SE detector have also been successful to generate material contrast in SOFC anodes or cathodes [4, 6, 11–14], because SE coefficients increase with decreasing electron energy and the effect of the work function of the material influences SE emission [12, 15]. However, sample charging and the resulting local change of work function greatly affects SE imaging. Even highly conductive materials like Ni, which is commonly used in SOFC anodes, can show pronounced changes in the SE yield depending on how well it is connected electrically [16]. Due to these difficulties, it was up to now not possible to achieve sufficient material contrast of the materials in all functional layers, i.e., cathode, anode and electrolyte, with one set of SEM imaging parameters.

In this study, the 3D structure of all functional SOFC layers was reconstructed covering a large volume of $3.5 \cdot 10^4 \mu\text{m}^3$ with a resolution in the few nm range. Standard SOFC materials are considered comprising YDZ and Ni for the cermet anode, YDZ for the electrolyte and LSM and YDZ for the cathode. SEM imaging conditions for the porous cermet anode and porous cathode were first optimized by a deterministic approach rather than trial-and-error tests. For this purpose Monte Carlo (MC) simulations were used, which are well established for the simulation of SE and BSE coefficients [17, 18]. We also have

analyzed the effect of the detection geometry of the different detectors and the influence of the collection angle range of BSEs on material contrast. Based on optimized parameters, FIB-SEM tomography experiments were performed with a state-of-the-art FIB-SEM instrument with four different SE and BSE detectors. We will demonstrate that the use of different SE and BSE detectors in a correlative way for simultaneous image acquisition within a single scan yields different intensities for all relevant phases and allows reliable segmentation of all primary and secondary phases.

2 Experimentals

2.1 Materials and Cell Fabrication

A-site deficient lanthanum manganite with the composition $(\text{La}_{0.8}\text{Sr}_{0.2})_{0.98}\text{MnO}_3$ (LSM) was used as cathode material. The electrolyte is composed of 8 mol.% Y_2O_3 -doped zirconia (YDZ) which was also added in the cathode and anode to increase the triple-phase boundary length. SOFC functional layers comprising a LSM cathode conduction layer (CCL), a LSM/YDZ cathode functional layer (CFL), a YDZ electrolyte and a Ni/YDZ cermet anode were screen printed on a green Zn-doped silicate substrate (Mg_2SiO_4) with a thickness of about $1,250 \mu\text{m}$. The whole cell was then co-sintered at temperatures between $1,100^\circ\text{C}$ and $1,300^\circ\text{C}$ in air. Pore formers were included in the substrate, CCL, CFL and anode to produce the desired porosity during co-sintering. The final thicknesses of functional layers were $70 \mu\text{m}$ (CCL), $16 \mu\text{m}$ (CFL), $15 \mu\text{m}$ (electrolyte) and $15 \mu\text{m}$ (anode). The cell was operated for a few hours in a test bench at 750°C with air on the cathode and hydrogen on the anode side. The fuel utilization was less than 5%. A cross-section elemental map of the whole SOFC was obtained by scanning electron microscopy – energy dispersive X-ray spectroscopy (SEM-EDXS) and is shown in Figure 1a. Different colors display the local intensities of the Mg–K, Zr–L, Ni–K, and La–L X-ray lines, which allow to identify different functional SOFC layers. The SE SEM image Figure 1b taken at 15 keV with the through-lens detector shows the same SOFC region, and it is obvious that the image intensity does not allow to distinguish different materials.

2.2 SEM Imaging and FIB-SEM Tomography

SOFC cells were cut using a diamond wire saw (Well Diamantdrahtsägen GmbH, Mannheim, Germany) and embedded into EpoFix epoxy resin (Struers A/S, Ballerup, Denmark) under vacuum conditions to infiltrate pores. The resin block was polished with diamond lapping film to obtain a clean edge for FIB cross-section preparation. To reduce charging, the sample surface was coated with 20 nm platinum in a Leica ACE600 (Leica Microsystems GmbH, Wetzlar, Germany) sputter coater. The area of interest was covered by a thick layer of platinum ($> 1 \mu\text{m}$) using subsequent electron-beam and ion-beam-induced deposition in a SEM/FIB Thermo Scientific™ Helios G4 FX DualBeam™ (Thermo Fisher Scienti-

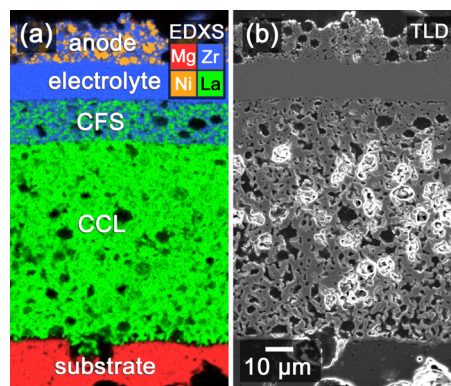


Fig. 1 SOFC cross-section prepared by focused-ion-beam milling. (a) Element mapping obtained by SEM-EDXS and (b) 15 keV secondary electron SEM image obtained with the through-lens detector of the same SOFC region. Scale bar in (b) applies to both images. (c) Scheme of Helios G4 FX instrument with different secondary and backscattered electron detectors used in this study.

fic, Waltham, Massachusetts, USA) instrument, which was also used for FIB-SEM tomography. A simplified scheme of the instrument including the SE and BSE detectors used within this study is depicted in Figure 1c. The through-lens detector (TLD) is a photomultiplier-tube based detector that is capable of detecting SEs or BSEs. The electrical potential of the mirror electrode and the suction tube can be adjusted to alter the detection characteristic of the TLD. More details of the TLD capabilities are outlined by Konvalina et al. [19]. In contrast to the previously mentioned detector, the concentric backscatter detector (CBS), mirror detector (MD) and in-column detector (ICD) are solid-state semiconductor detectors designed for capturing backscattered electrons. Image acquisition with in-column/in-lens detectors is particularly advantageous because these detectors can be used with the specimen immersed in the magnetic field of the objective lens (often referred to as immersion mode in the microscope software). This design reduces lens aberrations resulting in a smaller probe size and, therefore, a significant improvement in spatial resolution.

Element distributions were obtained by EDXS-SEM mappings. For this purpose, a Bruker (Bruker Corporation, Billerica, Massachusetts, USA) X-Flash 6 system in the Helios G4 FX was used. Acquisition and evaluation was performed with the Bruker ESPRIT 2.1 software.

In FIB-SEM tomography, the top sample surface is oriented perpendicular to the ion beam (52° stage tilt). A cross-section plane of the SOFC is polished to create a surface that can be imaged by the electron beam (cf. Figure 1c). To reduce mechanical movement of the stage, SEM images are typically recorded in tilted position. Resulting geometric distortions are removed by the microscope user interface. To prevent detector shadowing during SEM image acquisition, large trenches in the vicinity of the region of interest (ROI) were cut with a high Ga^+ -ion beam current (up to 65 nA). FIB-SEM tomography was performed by repeated SEM imaging and FIB milling leading to datasets of typically several hundred SEM images. Ga^+ -ion currents for FIB-SEM serial sectioning were set to 2.4 nA at 30 keV Ga -ion energy.

SEM images were recorded in immersion mode at eucentric working distance (approximately 4 mm). A total number of 416 consecutive slices with a slice thickness of 30 nm were recorded. The image stack was aligned by the Avizo software package (FEI, Version 9.2). Afterwards a 3D median and an anisotropic diffusion filter were applied to reduce image noise. Segmentation was carried out using the region-growing algorithm, described by Joos et al. [6]. Mesh generation and 3D visualization were conducted with Simpleware™ software (version P-2019.09; Synopsys, Inc., Mountain View, USA) and Blender (version 2.77; Blender Foundation, Amsterdam, Netherlands), respectively.

2.3 Monte Carlo Simulations

Monte Carlo (MC) electron-trajectory simulations are well established to study BSE and SE SEM image intensities [16, 18, 20, 21] and are therefore also well suited to optimize imaging conditions. MC simulations allow to take into account different material compositions, sample geometries, electron energies and detection parameters. MC simulations in this work were performed by the CASINO software package (v3.3.0.4) [22] for a primary electron energy range between 1 and 15 keV. 10^7 electron trajectories were simulated to accurately describe SE and BSE coefficients δ and η of all considered materials, which are determined by the ratio of simulated SEs and BSEs and the total number simulated trajectories. For 2D images, a lower number of simulated electrons (10^3 – 10^4) per pixel were used to reduce computation time. Input parameters for MC simulations are material properties (materials density, average atomic number, work function and plasmon energy) which are given in Table 1 for the materials relevant in this work. Due to the lack of data for the epoxy resin used to fill pores, parameters were assumed to be similar to EPON [23]. Mott cross-sections were selected in the simulation package to describe elastic scattering. SE coefficients were simulated using the dielectric function approach, which requires the knowledge of work function and plasmon energy of the simulated materials. Work function and plasmon energy for Ni are included in the CASINO software package. The work function for YDZ was taken from [24] and its plasmon energy was assumed to be the same as for ZrO_2 [25]. Plasmon energies for the other materials are not available in literature and, hence, their SE coefficients were not calculated.

It was taken into account in the simulations that the specimen surface is tilted by 38° with respect to the incident electron beam (52° stage tilt, cf. Figure 1c), which is a common configuration for FIB-SEM tomography experiments.

Table 1 Input parameters for Monte Carlo simulation of all materials contained in the investigated SOFC.

Phase	Stoichiometry	Density / g cm ⁻³	Average atomic number \bar{Z}	Work function / eV	Plasmon energy / eV
EPON [23]	H ₁₁₁ C ₁₁₅ O ₂₄	1.25	4.0		
YDZ	Zr _{0.84} Y _{0.16} O _{2-δ}	6.0	18.6	5.14 [24]	14.4 [25]
LSM	(La _{0.8} Sr _{0.2}) _{0.98} MnO _{3-δ}	6.5	20.3		
ZMO	ZnMn ₂ O ₄	5.2	16.0		
Ni	Ni	8.9	28.0	8.9	6.96
LSCF	La _{0.6} Sr _{0.4} Co _{0.2} Fe _{0.8} O _{3-δ}	6.3	19.9		
CGO	Ce _{0.9} Gd _{0.1} O _{3-δ}	7.2	34.5		
SZO	SrZrO ₃	5.4	20.4		

3 Results and Discussion

The investigated SOFC contains several materials, which require contrast optimization for reliable distinction and segmentation. For example, the material parameters of LSM and YDZ in the composite cathode are similar (cf. Table 1) and require imaging parameter optimization to achieve sufficient material contrast. MC simulations are therefore presented in Section 3.1 to investigate the influence of the electron energy on material contrast. In addition, the penetration depth of electrons is simulated to estimate expected resolution. Hereby we focus on the epoxy phase as its low material density suggests the highest penetration depth. Experimental results are presented in Section 3.2, which focus on the detection characteristics of different electron detectors in the Helios G4FX to further optimize contrast. This includes the effect of collection angle range of the used detectors on contrast formation to motivate why certain detectors are beneficial for achieving high material contrast. Finally, optimized imaging parameters and several detectors are used simultaneously to acquire a tomographic dataset of all functional SOFC layers. The images are segmented for phase assignment, consecutive 3D reconstruction and extraction of performance-relevant SOFC parameters.

3.1 Monte Carlo Simulations

3.1.1 Influence of Electron Energy on Material Contrast

The electron energy is an important parameter for material contrast in SEM imaging as shown by [16,26], and is determined by the SE coefficient δ and BSE coefficient η of the considered materials. MC simulations of electron trajectories were used to simulate η of common SOFC materials, relevant secondary phases and resin with properties given in Table 1. The results are shown in Figure 2a for electron energies between 1 and 15 keV. The SE coefficient shown in Figure 2b could only be determined for YDZ and Ni due to the lack of data for work functions and plasmon energies for the other materials.

According to Figure 2a, the BSE coefficients of several SOFC materials like YDZ, LSM, Ni and SrZrO₃ (SZO) are similar for a wide range of electron energies. In contrast, CGO (blue line), ZMO (red line) and epoxy (black line) differ significantly from the other materials, which is reasonable due to their large difference in average atomic number and material density. Apart from Ni, ZMO and epoxy, there is only a weak dependence of η on the electron energy for $E \geq 3$ keV which was also shown experimentally for other materials [27]. BSE coefficients for $E < 3$ keV either decrease or increase depending on the material composition. Figure 2b shows that SE emission for Ni and YDZ is most pronounced at low electron energies and quickly decays towards higher electron energies. The simulated SE coefficient of Ni agrees well with experimental data [16].

BSE image contrast C_{BSE} of two materials A, B with BSE coefficients η_A, η_B is defined by

$$C_{BSE} = \frac{\eta_A - \eta_B}{\eta_A} \quad (2)$$

Analogously, SE image contrast C_{SE} is defined by

$$C_{SE} = \frac{\delta_A - \delta_B}{\delta_A} \quad (3)$$

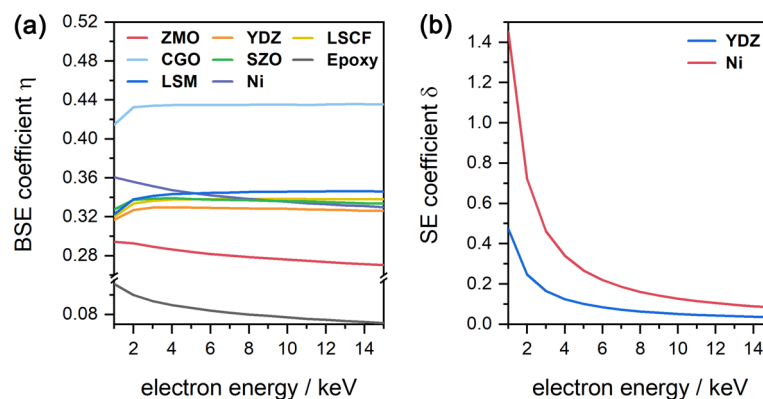


Fig. 2 MC simulations of (a) BSE and (b) SE coefficients for common SOFC materials, secondary phases and epoxy resin as a function of electron energy.

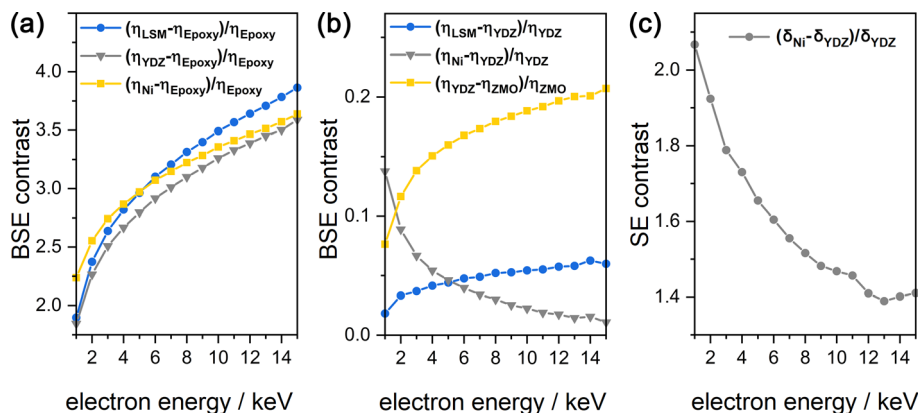


Fig. 3 Simulated (a,b) BSE and (c) SE image contrast for different material combinations (see legend) as a function of electron energy. For the sake of visibility, (a) BSE high-contrast and (b) BSE low-contrast material combinations were plotted separately. Lines are guide to the eye.

with SE coefficients δ_A , δ_B . Simulated BSE and SE material contrast is depicted in Figure 3 for different material combinations.

For the sake of clarity, only the BSE contrast of material combinations relevant in this study are presented. This includes LSM-epoxy, Ni-epoxy, YDZ-epoxy in Figure 3a and Ni-YDZ (anode), LSM-YDZ (cathode), YDZ-ZMO in Figure 3b. Interestingly, the BSE contrast increases with increasing electron energy for all material combinations except for Ni-YDZ (gray line in Figure 3b) with strongly decreasing BSE contrast towards higher electron energies. BSE contrast for LSM-YDZ is in general low (blue line in Figure 3b) as anticipated from similar materials properties. SE contrast of Ni-YDZ shown in Figure 3c also decreases with electron energy. We note, that SE contrast of Ni-YDZ is more than one order of magnitude higher compared to BSE contrast.

MC simulations were experimentally validated. For this purpose, BSE images of a CFL region containing LSM and YSZ were taken with the MD at 3, 5, 7, and 9 keV without changing amplifier settings of the BSE detector. The average image intensity of each phase was evaluated using ImageJ Fiji [28]. Image contrast of the phases was calculated based on the average image intensities I by

$$C_{img} = \frac{I_A - I_B}{I_A} \quad (4)$$

Since the brightness setting of the detector produces an arbitrary offset between measured image intensity and the number of detected electrons, only a qualitative comparison between experiment and simulation is possible. One also needs to be aware that the signal intensity of semiconductor BSE detectors depends not only on the number of detected electrons but also on their individual energies because the number of generated electron/hole pairs in semiconductor detectors depends on the electron energy. In addition, the simulated BSE coefficients do not account for the limited collection angle range of the employed BSE detector. The experimental image contrast is shown in Figure 4 as a function of the

electron energy. There is a reasonable agreement between experimental data and simulations, considering the above mentioned simplifications. The contrast between LSM and YDZ increases moderately between 3 and 9 keV, whereas there is a strong increase of contrast of LSM-epoxy and YDZ-epoxy.

After verification of the simulations by experimental results, we can conclude the following from the simulations. (i) BSE contrast increases for most material combinations with electron energy. (ii) This does not apply for Ni-YDZ where BSE contrast decreases with the electron energy.

(iii) SE contrast is high for this material combination but decreases also with electron energy. (iv) There is in general low BSE contrast for LSM-YDZ.

3.1.2 Penetration Depth of Electrons in Epoxy

The results of the preceding paragraph indicate that higher electron energies are preferable for high material contrast (apart from Ni-YDZ). However, a constraint on the choice of electron energy is set by the signal information depth. As BSEs can be generated at significant distance from the surface, materials with low material density and atomic number like epoxy resin become more transparent with increasing electron energy. Hence, small pores might be missed entirely. To characterize the information depth of BSEs in epoxy, the BSE coefficient of a sample composed of an epoxy film with varying film thickness on a YDZ substrate was simulated for different electron energies. A scheme of the model sample is shown in Figure 5a. The simulated line scan is indicated by the letter A. The BSE coefficient of epoxy η_{epoxy} is much lower compared to the BSE coefficient of YDZ η_{YDZ} , as already shown in Figure 2a.

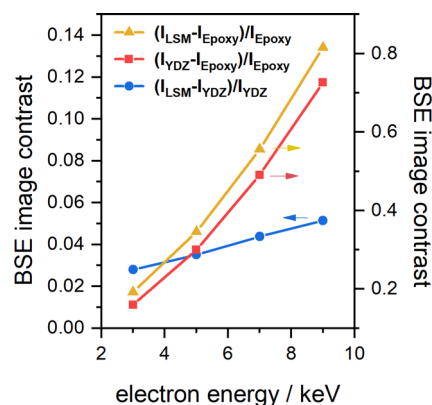


Fig. 4 Experimentally measured BSE contrast as a function of electron energy for different material combinations according to legend. Lines are guide to the eye.

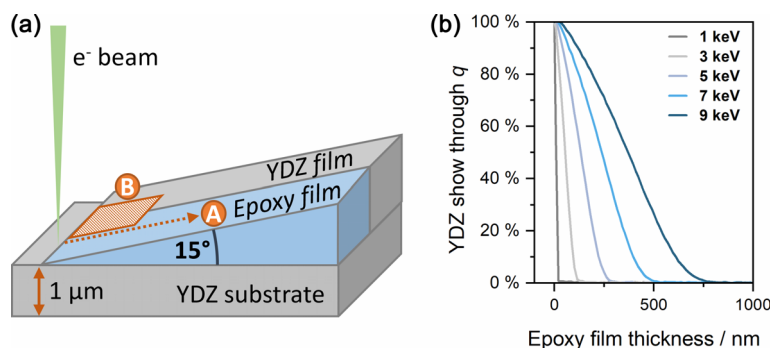


Fig. 5 (a) Scheme of the simulated sample geometry. The dotted red arrow (labelled A) corresponds to the scan direction of the simulated line profile with linearly increasing epoxy film thickness. The hatched rectangle (labelled B) visualizes the area used to simulate a BSE image. (b) Contribution of YDZ substrate to the BSE coefficient as a function of epoxy film thickness.

Table 2 Simulated information depth of BSE in epoxy.

Electron energy / keV	Information depth ($I = 1\%$) / nm	Critical thickness ($C_{BSE} = 5\%$) / nm
1	20	1
3	122	7
5	276	18
7	491	36
9	751	56

The simulated BSE coefficient at each scanning point (denoted as η_{film}) can indicate whether the signal is generated within the epoxy film or the underlying YDZ substrate, depending on whether it is closer to the known values of η_{YDZ} or η_{epoxy} . To quantify the contribution of the YDZ substrate to η_{film} denoted by q , the following normalization was used

$$q = \frac{\eta_{film} - \eta_{Epoxy}}{\eta_{YDZ} - \eta_{Epoxy}} \quad (5)$$

For $q = 0$ BSE are mainly generated within the epoxy film. If q reaches 1 most BSE are generated by the underlying YDZ substrate. The values of q as a function of epoxy film thickness are plotted in Figure 5b for electron energies between 1 and 9 keV. If $\eta_{film} \approx \eta_{epoxy}$ it is assumed that BSEs are mainly generated in the epoxy film. Hence, the epoxy film thickness where q reaches zero in Figure 5b corresponds to information depth. However, due to noise and the tail shape of the curve we consider the position where q reaches 1% as information depth. The information depth is given in Table 2 and ranges between 20.1 nm for 1 keV to 751 nm for 9 keV.

Hence, images of epoxy-filled pores taken at high electron energies

will display show-through effects of the underlying materials to the large information depth, e.g., 751 nm at 9 keV. However, this does not necessarily pose as a problem for image segmentation. This is demonstrated by simulated BSE images based on a model where next to the epoxy film a YDZ film with identical thickness is added. This geometry is illustrated in Figure 5a where the simulated image area is indicated with the letter B. Simulated BSE images are presented in Figure 6. As mentioned previously, show-through effects become increasingly pronounced with increasing electron energies and for small film thicknesses. In addition, the YDZ film at the interface appears brighter which can be explained by the reduced absorption of BSEs propagating through the epoxy film. *Vice versa*, the image intensity at the epoxy side of the interface appears slightly darker owing to the higher absorption probability of electrons propagating through the YDZ film. Even though show-through effects are visible for all electron energies, YDZ and epoxy can still be distinguished by their BSE intensity because there is still enough contrast between pure YDZ and epoxy on YDZ. If we assume that a BSE contrast C_{BSE} of 5% is sufficient for distinguishing both phases reliably, we can define a critical epoxy film thickness that can be used to estimate the depth resolution limit. The critical thickness ranges between 1.1 nm and 56.3 nm for electron energies between 1 and 9 keV (cf. Table 2) which is more than one order of magnitude below the information depth. If we assume a typical cubic voxel size of 20–30 nm, an electron energy of 5 keV or lower is mandatory. Hence, experiments were carried out at electron energies ≤ 5 keV.

intensity at the epoxy side of the interface appears slightly darker owing to the higher absorption probability of electrons propagating through the YDZ film. Even though show-through effects are visible for all electron energies, YDZ and epoxy can still be distinguished by their BSE intensity because there is still enough contrast between pure YDZ and epoxy on YDZ. If we assume that a BSE contrast C_{BSE} of 5% is sufficient for distinguishing both phases reliably, we can define a critical epoxy film thickness that can be used to estimate the depth resolution limit. The critical thickness ranges between 1.1 nm and 56.3 nm for electron energies between 1 and 9 keV (cf. Table 2) which is more than one order of magnitude below the information depth. If we assume a typical cubic voxel size of 20–30 nm, an electron energy of 5 keV or lower is mandatory. Hence, experiments were carried out at electron energies ≤ 5 keV.

3.2 FIB-SEM Tomography

3.2.1 Choice of Detector and Detector Parameters

BSE and SE images of the CFL taken at 3 keV with different detectors are depicted in Figures 7a–d with intensity histograms below the SEM images. To verify phase assignment in this region, a color-coded element distribution of Mn (LSM, red) and Zr (YDZ, blue) obtained by EDXS-SEM mapping is presented in Figure 7e.

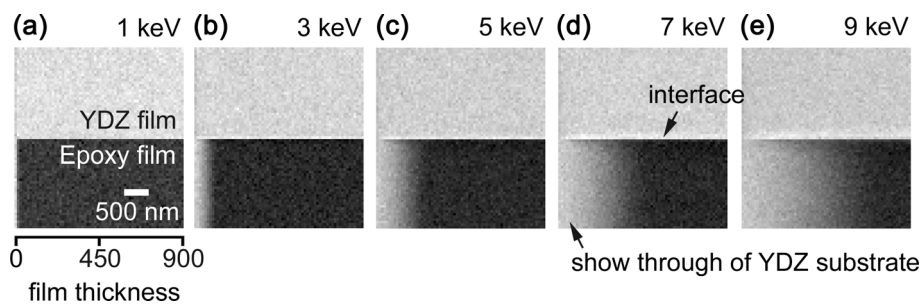


Fig. 6 Simulated BSE images of a YDZ and epoxy film with varying film thickness on a YDZ substrate. The electron energy was set to (a) 1 keV, (b) 3 keV, (c) 5 keV, (d) 7 keV, and (e) 9 keV. The scale bar in (a) applies to all images. The simulated geometry is shown in Figure 5a and highlighted with the letter B.

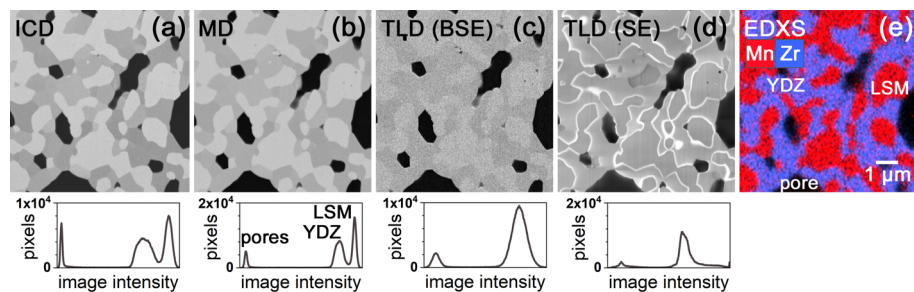


Fig. 7 Images of the same CFL region. BSE images taken at 3 keV with different detectors (a) ICD, (b) MD, and (c) TLD in BSE mode; (d) is a 3 keV SE image taken with the TLD detector in the SE mode; (e) EDXS-SEM mapping obtained at 5 keV displaying the X-ray intensity of the Mn-K (red) and Zr-L (blue) X-ray lines. The scale bar in (e) applies to all images.

It is obvious that all three phases can be distinguished by BSE imaging (cf. Figures 7a–c). The bright gray phase can be assigned to LSM. The dark gray phase corresponds to YDZ and the epoxy-filled pores show black contrast as predicted by the simulated BSE coefficients (cf. Figure 2a). The histograms of the ICD and MD micrographs show separate peaks for YDZ, LSM and epoxy-filled pores. This is not the case for the image in Figure 7c taken with the TLD in the BSE mode. Here, the histogram does not show separate peaks for LSM and YDZ due to the weak contrast of the phases.

We note, the YDZ peak in the histogram of the ICD image (cf. Figure 7a) is broadened compared to the MD image. This effect is associated with grain orientation contrast because electron channeling is more pronounced compared to the MD image. Apparently, channeling is stronger for YDZ compared to LSM. The small collection angle range of the ICD, which is located in uppermost position in the electron column (cf. Figure 1c), collects only electrons with scattering angles close to 180° . Hence, coherent elastic scattering is most pronounced leading to an enhanced sensitivity towards orientation changes of the crystalline lattice. In contrast, the MD covers a wider scattering angle range and, therefore, a larger number of multiple-scattered electrons are collected leading to slightly reduced crystal-orientation sensitivity compared to the ICD. Unfortunately, the image intensity in ICD images is inhomogeneous for a large field-of-view as, e.g., seen in Figure 12a, which is not observed in MD images. Hence, MD images are best suited for threshold-based image segmentation algorithms.

LSM and YDZ cannot be distinguished in the SE image taken at 3 keV with the TLD in the SE mode (Figure 7d). Instead, strong bright charging fringes are observed even at low electron currents (≤ 50 pA). Charging is not surprising due to the poor electrical conductivity of YDZ. However, depending on the electron energy, charging fringes can be reduced and a reasonable contrast between YDZ and LSM can be

achieved. Such an example is presented in the SE image Figure 8a, which was recorded with the TLD in SE mode at 5 keV and 0.8 nA electron beam current. The high image intensity of YDZ can be explained by negative charging. As the electrical conductivity of LSM is several orders of magnitude higher than in YDZ [29,30], charges do not build up in LSM grains as electrons can move *via* the percolating LSM network. However, if LSM grains are electrically isolated, negative charging in combination with a strong increase in image intensity is visible.

Figures 8a and 8b represent two consecutive slices acquired during a FIB-SEM tomography experiment where the connection of one LSM grain to the rest of the LSM network was interrupted. This leads to strong charging for the disconnected grain resulting in a contrast inversion between LSM and YDZ. This might lead to erroneously assigned phases during image segmentation. In contrast, images taken simultaneously with the MD do not show any contrast inversion, as shown in Figures 8c and 8d. A similar observation was already made for Ni/YDZ anodes where percolating and non-percolating Ni grains can be distinguished by their image contrast [16].

BSE images are also capable of revealing additional phases that can not be distinguished in SE images. In our previous work, it was shown that co-sintered SOFCs contain secondary phases, e.g., ZMO [31]. This phase cannot be reliably detected by SE detectors because it shows a similar image intensity as LSM (cf. Figure 8e). In contrast, ZMO is clearly visible in the BSE image taken at 5 keV with the MD detector (Figure 8f) because it has a considerably lower BSE coefficient compared to LSM or YDZ (cf. MC simulations in Figure 2a). The corresponding histogram shows separate peaks for all phases.

ICD and TLD images of the cermet Ni/YDZ anode are presented in Figures 9a–d. The images are recorded with an electron energy of 3 keV with their intensity histograms shown below the images. A SEM-EDXS mapping with the color-

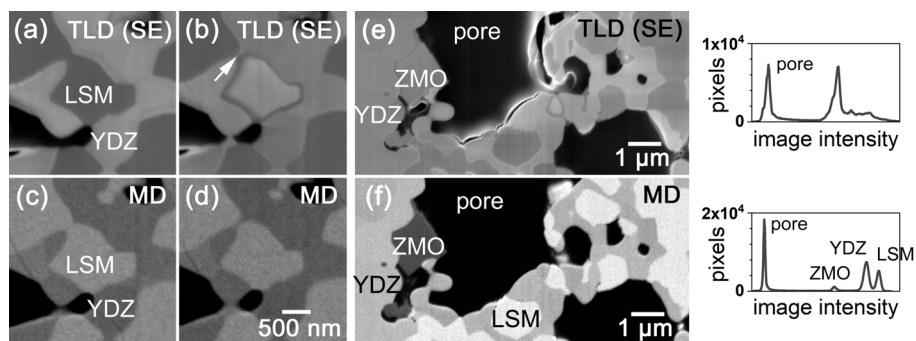


Fig. 8 (a, b) TLD (SE) and (c, d) MD images of two consecutive FIB slices. Percolated and non-percolated LSM show different contrast for SEs recorded with the TLD. (e) TLD (SE) and (f) MD image of region containing ZMO as secondary phase and corresponding histograms. The scale bar in (d) applies to (a), (b), and (c). All images were taken at 5 keV electron energy.

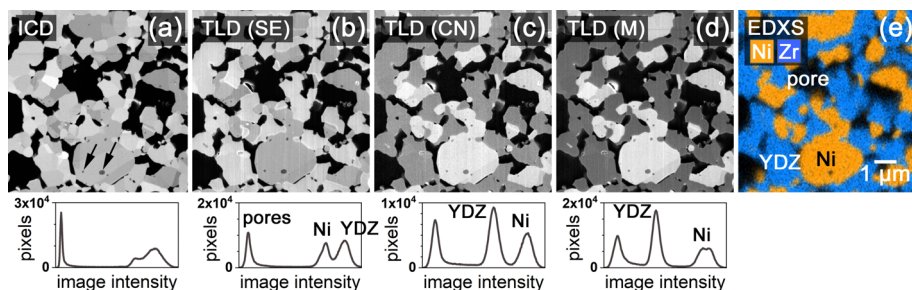


Fig. 9 Images of a SOFC Ni/YDZ cermet anode taken at 3 keV with the (a) ICD and TLD in (b) SE mode, (c) charge-neutralization mode, and (d) manual mode. A corresponding EDXS mapping with the color-coded Ni-L and Zr-L line intensity is given in (e). The scale bar in (e) applies to all images.

coded Ni-L and Zr-L line intensities in Figure 9e was used for phase assignment. BSE images turned out to be insufficient to distinguish Ni and YDZ for a wide range of electron energies and various BSE detectors. This is exemplified by the image acquired with the ICD (cf. Figure 9a), where Ni and YDZ cannot be unambiguously separated as shown by the strong overlap of the image intensities of Ni and YDZ in the histogram. Pronounced channeling contrast is observed especially for Ni, which is the main reason for the poor material contrast. In contrast to the MC simulations (Figure 2a), the image intensity of Ni appears lower compared to YDZ. This discrepancy can be attributed to the fact that MC simulations do not take into account Bragg contrast induced by coherent electron scattering. We note, that the dark precipitates within the Ni grains (example marked by white arrows in Figure 9a) correspond to a Mn-rich secondary phase that is formed during sample fabrication. More details about this phase can be found elsewhere [31].

Using instead SE imaging with the TLD results in reasonable contrast between Ni and YDZ (cf. Figure 9b). However, strong charging of YDZ does not provide stable image contrast as the image intensity of YDZ increases over time. To avoid charging induced contrast, the TLD can be operated in charge neutralization mode (CN) where the suction tube is set to 0 V and the mirror electrode to -15 V (cf. Figure 1b). A TLD image recorded with the TLD detector operated in CN mode is displayed in Figure 9c. The strong contrast between YDZ and Ni is also reflected by clearly separated YDZ and Ni peaks in the histogram. Compared to the image in standard SE mode Figure 9b, the contrast between Ni and YDZ is inverted which is likely to be induced by the absence of charging-induced intensity contributions for YDZ. Image contrast can be further improved by increasing the suction tube voltage and further decreasing the voltage of the mirror electrode in the manual mode (M) to 244.7 V and -50 V, respectively. An image recorded with these parameters is shown in Figure 9d. With these settings reliable segmentation based on image thresholding is possible.

3.2.2 Influence of Detection Angle Range on Material Contrast

The concentric backscatter (CBS) detector (cf. Figure 1c and schematic drawings in Figures 10a–d) was used to study the effect of the collection angle range on BSE image contrast for the CFL. The CBS contains four concentric ring-shaped segments that can be separately selected to contribute to image formation. The inner-most segment ring (segment A) collects electrons which are almost fully backscattered,

i.e., the scattering angle is close to 180° with respect to the incident electrons. We adopt the notation that the scattering angles are small with respect to the optical axis of the system. Accordingly, the outermost ring detects electrons scattered in comparatively high angles (segment D).

Figure 10 shows BSE images acquired with only one ring segment activated. For low collection angles (segment A, $11\text{--}18^\circ$, cf. Figure 10a), good contrast between LSM and YDZ is observed as visualized by two separated peaks in the corresponding histogram. Larger collection angles (segment C, $28\text{--}36^\circ$) reduce material contrast as highlighted by the region in the red circle in Figures 10a–c where phase assignment becomes increasingly ambiguous even resulting in complete disappearance of material contrast (segment D, $37\text{--}44^\circ$, cf. Figure 10d). In addition, topographic features as FIB-induced trenches (cf. red arrow in Figures 10a and 10b) become more and more pronounced. This is reasonable as electrons scattered in larger angles are usually generated close to the surface [32] and can be used for surface topography imaging [33]. Hence, detectors with low collection angles are beneficial to obtain high material contrast and even reduce contributions of topographic features like FIB trenches.

This is further illustrated by systematically increasing the working distance and therefore decreasing the collection angles without changing any other microscope parameter. The contrast between YDZ and LSM obtained by the CBS (segment A) detector increases with decreasing collection angles

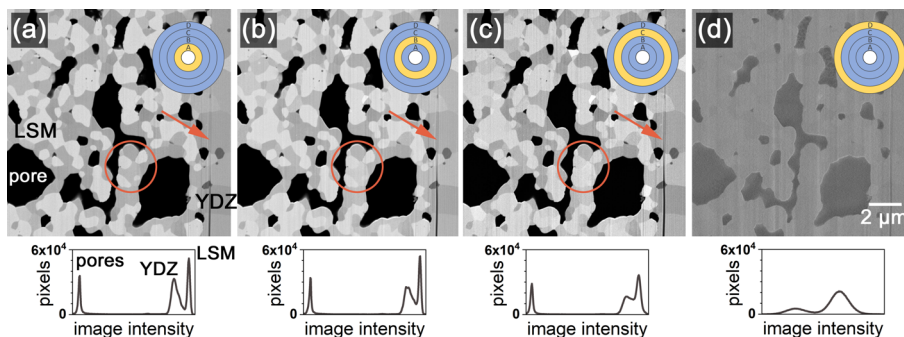


Fig. 10 3 keV BSE images of the same CFL sample region taken with the (a) inner-most segment A (collection angle $11\text{--}18^\circ$), (b) second inner segment B (collection angle $19\text{--}27^\circ$), (c) second outer segment C (collection angle $28\text{--}36^\circ$) and (d) outer-most segment D (collection angle $37\text{--}44^\circ$) of the CBS detector. Corresponding histograms are given below each image.

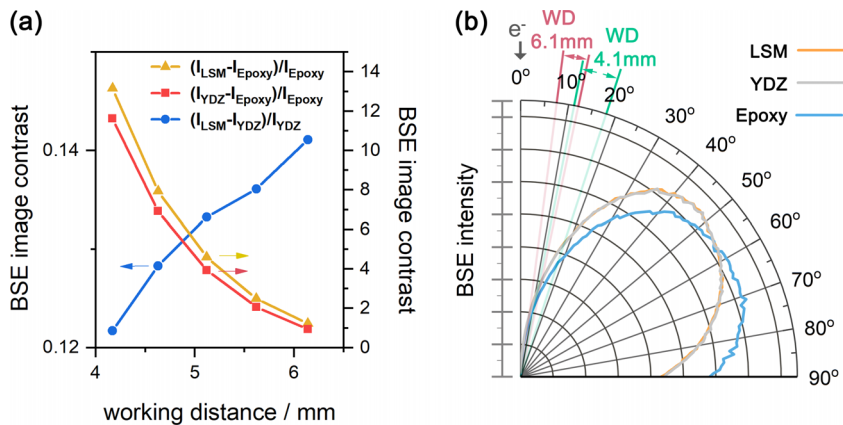


Fig. 11 (a) Measured BSE image contrast as a function of working distance for 3 keV BSE images generated with the CBS A segment. A higher working distance (WD) corresponds to smaller detector collection angles. Note that the left ordinate corresponds BSE contrast of LSM/YDZ while the right ordinate corresponds to LSM/epoxy and YDZ/epoxy contrast. (b) Simulated angular distribution of BSEs with collection angle range indicated for 6.1 and 4.1 mm working distances. 0° corresponds to the incident direction of the electrons. Note, that the LSM intensity curve (orange) is superimposed by the YDZ scattering characteristics (gray).

(cf. blue line in Figure 11a). However, image contrast between epoxy and YDZ/LSM drops significantly by more than one order of magnitude. This effect can be understood by the angular distribution of BSE obtained by MC simulations (cf. Figure 11b) where the angular scattering characteristics of LSM, YDZ and epoxy are shown by blue, gray and orange lines. The incident electron beam corresponds to an angle of 0°. Interestingly, the angular BSE distribution of LSM and YDZ is almost identical (overlapping gray and orange lines in Figure 11b) explaining the poor contrast between these materials and the weak dependence on the collection angle. The geometrically estimated CBS collection angle range of segment A at two different working distances is marked in Figure 11b. For working distance of 4.1 mm, the signal intensity of epoxy and LSM (or YDZ) collected by the CBS detector differs significantly. However, with decreasing collection angles and increasing working distance, the BSE intensity of the materials converge and image contrast decreases in agreement with the experimental results.

3.2.3 Correlative FIB-SEM Reconstruction with Optimized Parameters

All functional layers of the investigated SOFC were reconstructed with a tomographic dataset that was recorded with a voxel size of $15 \times 15 \times 30 \text{ nm}^3$ at 3 keV electron energy and an electron beam current of 0.8 nA. Images were taken simultaneously with three different detectors (ICD, MD and TLD). As outlined previously, the TLD was operated in

manual mode with the optimized parameters given in Section 3.2.2. Three images from one example slice of the dataset is shown in Figures 12a–c. BSE images recorded with the ICD or MD (Figures 12a and 12b) show pronounced contrast for all cathode phases but insufficient contrast for the anode. The SE image Figure 12c recorded with the TLD is well suited to distinguish the anode phases Ni and YDZ but shows low contrast for cathode phases. Hence, segmentation was carried out using the TLD signal for the anode phases. The MD signal was used for segmenting cathode phases rather than the ICD signal because the latter one shows intensity gradients over the analyzed field of view. However, the ICD signal can be used for refinement in cases of ambiguous contrast due to its overall higher material contrast. TLD and MD images were segmented using the region growing algorithm as described in

[6]. Segmented TLD and MD images were combined (cf. green and yellow frames in Figures 12b and 12c) to display all phases in a single image (cf. Figure 12d). This procedure was carried out for the whole tomographic image stack.

The stack of segmented images after 3D reconstruction and rendering is shown in Figure 13a with a large total volume of $38 \times 83 \times 11 \mu\text{m}^3$. Individual phases, e.g., the secondary phase ZMO (green regions) can be investigated regarding its distribution within the SOFC structure. In Figure 13b only ZMO in green regions is shown. YDZ set transparent to enhance ZMO visibility. It is obvious that the ZMO phase is mainly contained in the CCL and less frequent in the CFL. In addition, ZMO precipitates are accumulated at the cathode–electrolyte interface but do not completely block oxygen-ion transport across the interface.

For a segmented image stack, various microstructure parameters of the reconstructed functional SOFC layers can be

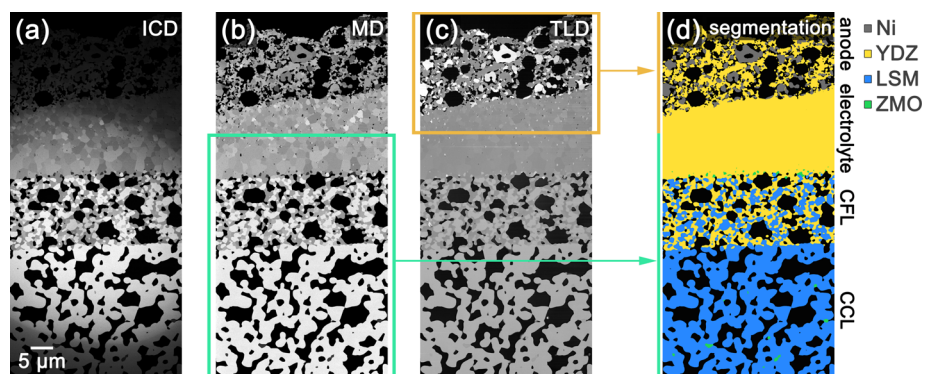


Fig. 12 (a–c) Example images acquired during a FIB-SEM tomography experiment with (a) ICD, (b) MD, and (c) TLD. All images were recorded simultaneously with a primary electron energy of 3 keV. (d) shows the segmented image with Ni marked in gray, YDZ in yellow, LSM in blue and ZMO in green. The scale bar in (a) applies to all images. (d) is obtained by combining segmented regions from the MD image (green frame) and the TLD image (yellow frame).

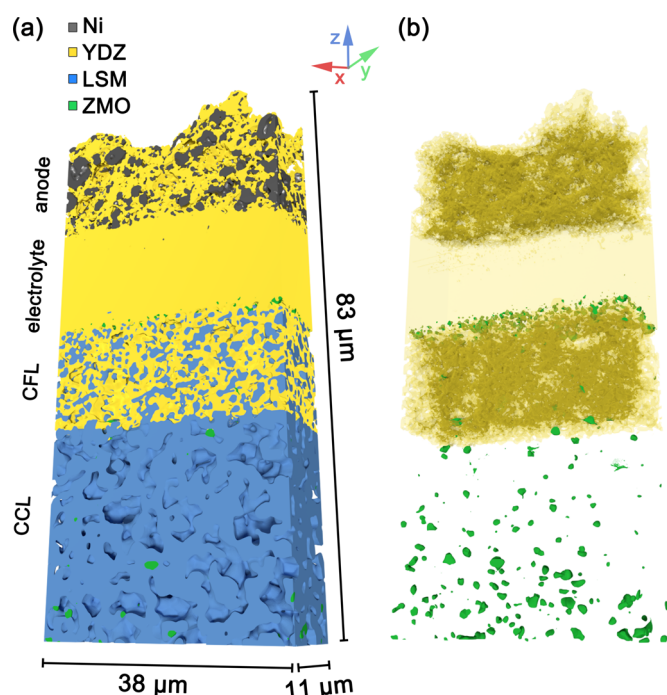


Fig. 13 (a) 3D rendering of the reconstructed SOFC volume with color-coded phases YDZ, LSM, Ni, and ZMO; (b) 3D rendering (same scale as in (a)) of the secondary phase ZMO to visualize its distribution within the SOFC. The YDZ phase is rendered semi-transparent.

calculated. Some of these parameters can be directly related to cell performance like the tortuosity factor τ , describing the increase of diffusion losses compared to direct diffusive transport. Considering that only one phase with an intrinsic diffusivity of D_{in} contributes to diffusive transport, the effective diffusivity of a heterogeneous system D_{eff} can be described by

$$D_{eff} = D_{in} \frac{\varepsilon}{\tau} \quad (6)$$

where ε accounts for the volume fraction of the phase contributing to diffusion transport.

Parameters (except the triple-phase boundary (TPB)) were calculated for the anode, CCL and CFL using the software

package TauFactor [34]. The TPB length was calculated using the centroid method and only included actively connected TPBs. The calculated data of volume fraction, percolation and tortuosity of the different phases as well as TPB length are summarized in Table 3. The evaluated data shows that the porosity in the CCL and CFL are identical while it is somewhat larger in the anode. Percolation is close to 100% in the cathode. However, it is noteworthy that the Ni network shows a comparatively poor percolation (90%), which makes electrical breakdown likely during extended operation at high temperatures by Ni grain coarsening. Poor Ni percolation goes along with a large tortuosity which is considerable higher compared to other cell designs [14,35,36]. In a forthcoming publication, the parameters in Table 3 will be used to model the electrochemical performance of the cell.

4 Summary and Conclusions

3D microstructural data obtained by FIB-SEM tomography facilitate the understanding of cell performance, fabrication parameters and aging-related phenomena. However, SEM images for FIB-SEM tomography require sufficient material contrast of all materials of interest for reliable segmentation before 3D reconstruction. In this work we succeeded to simultaneously acquire SEM images with different secondary electron (SE) and backscattered electron (BSE) detectors, which allow to image all material phases in functional SOFC layers with high material contrast within a single scan. The investigated cell was composed of a Ni/Y₂O₃-doped ZrO₂ (YDZ) cermet anode, YDZ electrolyte and (La,Sr)MnO₃/YDZ cathode. With the correlative use of BSE and SE images a segmentation of all electrochemically active cell components was achieved and performance relevant microstructural data as tortuosity and triple phase boundary length were extracted for both anode and cathode. The data revealed poor percolation of the Ni phase within the cermet anode of the analyzed SOFC.

Monte Carlo (MC) electron trajectory simulations were shown to be an effective tool to model the complex relationship between material composition, primary electron energy

Table 3 Calculated SOFC parameters volume fractions, triple phase boundary lengths (TPI), percolations and tortuosities for the CCL, CFL and anode based on FIB-SEM reconstruction.

Phase	CCL			CFL			Anode		
	LSM	ZMO	Pore	LSM	YDZ	Pore	Ni	YDZ	Pore
Volume fraction / %	64	0.5	35	29	37	34	24	34	42
TPB density / μm^{-2}				1.6			3.5		
Directional percolation x / %	100	–	99.8	96.2	99.8	99.5	89.0	99.8	99.8
Directional percolation y / %	100	–	99.8	96.2	99.8	99.5	89.0	99.8	99.8
Directional percolation z / %	100	–	99.8	96.2	99.8	99.5	89.0	99.8	99.8
Tortuosity x	1.4	∞	3.1	9.4	2.4	4.9	>10	2.8	3.5
Tortuosity y	1.4	∞	2.9	8.3	2.4	3.8	>10	2.7	3.1
Tortuosity z	1.5	∞	2.9	8.9	2.4	4.3	>10	2.8	3.3

and SEM image contrast. BSE contrast for most relevant SOFC material combinations increases with electron energy with the exception of Ni-YDZ in the cermet anode where the opposite behavior is observed. Selection of higher electron energies is limited by the increasing electron penetration depth leading to the reduction of lateral resolution.

In contrast to cathode materials, BSE contrast of the Ni-YDZ cermet anode is generally poor due to strong channeling contrast which is not considered by Monte Carlo simulations. However, SE imaging provides high Ni-YDZ contrast which was further optimized by using build-in electrodes in the Helios G4FX for precise tuning of the SE detection characteristics to effectively reduce charging.

Focusing on the detection parameters of BSE/SE detectors of a state-of-the-art Helios G4FX provided additional insights on how to further optimize material contrast. For the cathode, BSE detectors were shown to be superior compared to SE detectors because SE contrast strongly depends on the percolation of individual LSM particles due to charging. In addition, secondary phases like ZMO can be distinguished reliably due to pronounced material contrast, which is not possible for SE detection. Systematic analysis of the BSE detector collection angle demonstrates that detectors with extremely low collection angles are more suitable for capturing material contrast because the signal is mainly composed of coherently elastically scattered electrons. However, MC simulations show that exceptions may exist where lower collection angles can also reduce the material contrast, e.g., between epoxy and YDZ.

Simultaneously acquisition of SE and BSE images with an optimized electron energy opens up opportunities of generating high material contrast for several materials of interest. By avoiding multiple scans of the same slice with different parameters, we eliminate sample drift and significantly reduce the overall acquisition time for tomographic image stacks. This facilitates a substantial increase of the analyzed volume and enhances the relevance of the extracted material parameters.

Acknowledgements

The authors gratefully acknowledge funding by the Federal Ministry for Economic Affairs and Energy (BMW, 03ET6101B and 03ET6101A). Open access funding enabled and organized by Projekt DEAL.

Data Availability Statement

Data available on request from the corresponding author.

References

- [1] K. Huang, J. B. Goodenough, *Solid oxide fuel cell technology. Principles, performance and operations*, Woodhead Publishing Ltd., Cambridge, United Kingdom, **2009**, Vol. 11.
- [2] J. R. Wilson, W. Kobsiriphat, R. Mendoza, H.-Y. Chen, J. M. Hiller, D. J. Miller, K. Thornton, P. W. Voorhees, S. B. Adler, S. A. Barnett, *Nat. Mater.* **2006**, *5*, 541.
- [3] F. Wankmüller, J. Szász, J. Joos, V. Wilde, H. Störmer, D. Gerthsen, E. Ivers-Tiffée, *J. Power Sources* **2017**, *360*, 399.
- [4] J. A. Taillon, C. Pellegrinelli, Y.-L. Huang, E. D. Wachsmann, L. G. Salamanca-Riba, *Ultramicroscopy* **2018**, *184*, 24.
- [5] J. Scott Cronin, K. Muangnapoh, Z. Patterson, K. J. Yakal-Kremiski, V. P. Dravid, S. A. Barnett, *J. Electrochem. Soc.* **2012**, *159*, B385.
- [6] J. Joos, M. Ender, I. Rotscholl, N. H. Menzler, E. Ivers-Tiffée, *J. Power Sources* **2014**, *246*, 819.
- [7] M. Kubota, T. Okanishi, H. Muroyama, T. Matsui, K. Eguchi, *J. Electrochem. Soc.* **2015**, *162*, F380.
- [8] J. Wilson, J. S. Cronin, S. Rukes, A. Duong, D. Mumm, S. A. Barnett, *ECS Trans.*, **2009**, *25*, 283.
- [9] G. J. Nelson, W. M. Harris, J. J. Lombardo, J. R. Izzo Jr., W. K. S. Chiu, P. Tanasini, M. Cantoni, J. Van herle, C. Comninellis, J. C. Andrews, Y. Liu, P. Pianetta, Y. S. Chu, *Electrochem. Commun.* **2011**, *13*, 586.
- [10] A. Z. Lichtner, D. Jauffrès, D. Roussel, F. Charlot, C. L. Martin, R. K. Bordia, *J. Eur. Ceram. Soc.* **2015**, *35*, 585.
- [11] J. Nielsen, P. S. Jørgensen, *Electrochim. Acta* **2017**, *252*, 387.
- [12] N. Vivet, S. Chupin, E. Estrade, A. Richard, S. Bonnamy, D. Rochais, E. Bruneton, *J. Power Sources* **2011**, *196*, 9989.
- [13] S.-S. Liu, A. Takayama, S. Matsumura, M. Koyama, *J. Microsc.* **2016**, *261*, 326.
- [14] O. M. Pecho, O. Stenzel, B. Iwanschitz, P. Gasser, M. Neumann, V. Schmidt, M. Prestat, T. Hocker, R. J. Flatt, L. Holzer, *Materials* **2015**, *8*, 5554.
- [15] J. Cazaux, *J. Appl. Phys.* **2011**, *110*, 24906.
- [16] K. Thydén, Y. L. Liu, J. B. Bilde-Sørensen, *Solid State Ionics* **2008**, *178*, 1984.
- [17] Z.-J. Ding, R. Shimizu, *Scanning* **1996**, *18*, 92.
- [18] R. Gauvin, P. Hovington, D. Drouin, *Scanning* **1995**, *17*, 202.
- [19] I. Konvalina, F. Mika, S. Krátký, E. Materna Mikmeková, I. Müllerová, *Materials* **2019**, *12*, 2307.
- [20] Z. J. Ding, H. M. Li, *Surf. Interface Anal.* **2005**, *37*, 912.
- [21] T. Kowoll, E. Müller, S. Fritsch-Decker, S. Hettler, H. Störmer, C. Weiss, D. Gerthsen, *Scanning* **2017**, *2017*, 1.
- [22] H. Demers, N. Poirier-Demers, A. R. Couture, D. Joly, M. Guilmain, N. de Jonge, D. Drouin, *Scanning* **2011**, *33*, 135.
- [23] M. Pfaff, E. Müller, M. F. G. Klein, A. Colsmann, U. Lemmer, V. Krzyzaneck, R. Reichelt, D. Gerthsen, *J. Microsc.* **2011**, *243*, 31.
- [24] D. Tsiplakides, C. G. Vayenas, *Electrochim. Acta* **2001**, *148*, E189.
- [25] L. K. Dash, N. Vast, P. Baranek, M.-C. Cheynet, L. Reining, *Phys. Rev. B: Solid State* **2004**, *70*, 44.
- [26] I. Müllerová, L. Frank, *Scanning* **2004**, *26*, 18.

- [27] L. Reimer, C. Tollkamp, *Scanning* **1980**, 3, 35.
- [28] J. Schindelin, I. Arganda-Carreras, E. Frise, V. Kaynig, M. Longair, T. Pietzsch, S. Preibisch, C. Rueden, S. Saalfeld, B. Schmid, J.-Y. Tinevez, D. J. White, V. Hartenstein, K. Eliceiri, P. Tomancak, A. Cardona, *Nat. methods* **2012**, 9, 676.
- [29] Y.-G. Jung, J. Choi, Y. Yoon, D. Shin, *J. Nanosci. Nanotechnol.* **2011**, 11, 7475.
- [30] J. Garcia-Barriocanal, A. Rivera-Calzada, M. Varela, Z. Sefrioui, E. Iborra, C. Leon, S. J. Pennycook, J. Santamaria, *Science* **2008**, 321, 676.
- [31] J.-C. Njodzefon, N. Maier, J. Schmieg, M. Meffert, H. Störmer, D. Gerthsen, P. Lupetin, *Proceedings of the 13th European SOFC & SOE Forum 2018, Lucerne, Switzerland. Advanced characterization techniques I+II* (Ed. E. Ivers-Tiffée), European Fuel Cell Forum AG, **2018**, 1.
- [32] D. C. Joy, *J. Microsc.* **1991**, 161, 343.
- [33] Q. Wan, R. A. Plenderleith, M. Dapor, S. Rimmer, F. Claeysens, C. Rodenburg, *J. Phys.: Conf. Ser.* **2015**, 644, 12018.
- [34] S. J. Cooper, A. Bertei, P. R. Shearing, J. A. Kilner, N. P. Brandon, *SoftwareX* **2016**, 5, 203.
- [35] L. Holzer, B. Iwanschitz, T. Hocker, L. Keller, O. Pecho, G. Sartoris, P. Gasser, B. Muench, *J. Power Sources* **2013**, 242, 179.
- [36] M. Trini, P. S. Jørgensen, A. Hauch, J. J. Bentzen, P. V. Hendriksen, M. Chen, *J. Electrochem. Soc.* **2019**, 166, F158.